Article

Long-Range Interatomic Coulombic Decay in ArXe Clusters: Experiment and Theory

Marko Förstel,[†,×] Melanie Mucke,[†,#] Tiberiu Arion,[†,∇] Toralf Lischke,[†] Markus Pernpointner,[‡] Uwe Hergenhahn,[*,⊥,§] and Elke Fasshauer[*,∥]

[†]Max-Planck-Institute for Plasma Physics, Boltzmannstraße 2, D-85748 Garching, Germany

[‡]Theoretical Chemistry, University of Heidelberg, Im Neuenheimer Feld 229, D-69120 Heidelberg, Germany

[⊥]Leibniz Institute of Surface Modification, Permoserstraße 15, D-04318 Leipzig, Germany

[§]Max-Planck-Institute for Plasma Physics, Wendelsteinstraße 1, D-14791 Greifswald, Germany

[∥]Centre for Theoretical and Computational Chemistry, Department of Chemistry, University of Tromsø—The Arctic University of Norway, N-9037 Tromsø, Norway

Ⓢ Supporting Information
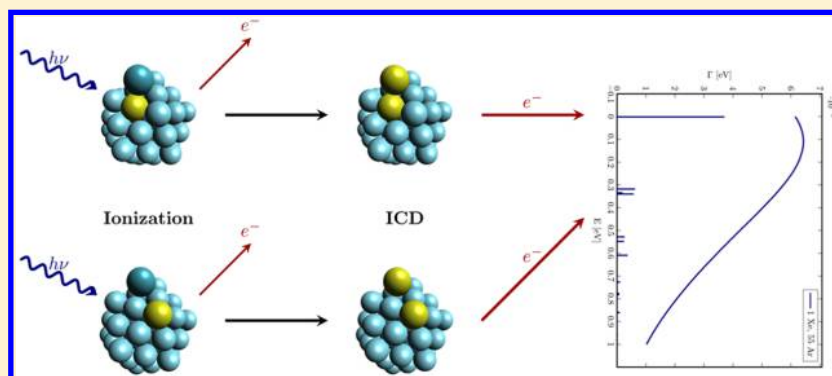
ABSTRACT: We report autoionization channels of Ar inner valence ionized states in mixed ArXe clusters and compare our experimental data obtained by electron–electron coincidence spectroscopy to our theoretical simulations for representative cluster structures. The combined experimental and theoretical data show that the autoionization of Ar $3s^{-1}$ in ArXe is dominated by interatomic coulombic decay (ICD) to Xe atoms in the second and higher coordination shells of the originally excited atom. Clusters with a range of sizes, compositions, and structures were probed. The Xe content in the clusters was varied between 10% and 53%. Besides ICD, also electron transfer mediated decay (ETMD(3)) was found important in many of the calculated spectra, although it is seen with less intensity in the experimental spectra. From the calculations, we identify structural motifs in which the ETMD rate is minimized vs the ICD rate and suggest that these are preferentially realized in our experiment, in which clusters are formed by supersonic expansion of an Ar–Xe mixture. Suggested cluster structures either feature a clear segregation between Ar and Xe fractions, e.g., Xe core–Ar shell systems, or contain a few Xe atoms singled out at surface sites on an Ar cluster. These structures differ significantly from the majority of calculated minimum energy structures for ArXe systems of 38 atoms, which might show that the latter, annealed structures are not realized in our experiment. We show experimentally that the relaxation of Ar inner valence states by ICD and ETMD together has an efficiency of unity, within the experimental accuracy, for all clusters probed, except those with the lowest Xe content. The outer valence photoelectron spectra of ArXe are discussed also.

■ INTRODUCTION

Electron spectroscopy can make important contributions to the research on composition and structure of free nanoparticles.[1] Besides photoionization, free electrons emerging from nanoparticles can also be produced by the relaxation of electronically excited states. One such process, which is of particular relevance in weakly bonded systems, is the interatomic or intermolecular coulombic decay (ICD).[2] In ICD, an electronic excitation decays by energy transfer to one of its neighboring atoms or molecules, thus releasing a free electron from the latter site. ICD is an important relaxation channel, e.g., for

inner-valence holes in atoms, and also for core level vacancies, e.g., in H_2O, where it competes with Auger decay.[3]

By definition, ICD is particularly sensitive to the chemical environment of the atom or molecule in which the primary excitation has taken place. We suggest that this property of ICD decay spectra can be used to derive information on a nanoparticle or a solvation system. The term "excitation" is

used here in a broader sense—in the systems we consider in this work, ICD occurs from an excited, singly charged Ar state created by photoionization. In other systems, ICD was also observed from neutral excited states and states with more than one vacancy.

We report here studies in which we produced heterogeneous clusters of the noble gases Ar and Xe with different sizes, and with compositions ranging from a few Xe dopant atoms in an Ar matrix to clusters containing an equal amount of both species. By the use of electron–electron coincidence spectroscopy and of theoretical simulations on prototypical systems, we show how the radiationless decay spectrum of Ar inner valence (3s) ionized states connects to the structure of the clusters.

Intermolecular coulombic decay initially was predicted from theoretical considerations of the energy levels in singly vs doubly ionized, and doubly vs triply ionized, hydrogen-bonded clusters.[2] The first experimental work some years later used Ne clusters,[4,5] but quickly was followed by demonstrations of ICD in a diverse range of other systems. Experimental and theoretical progress has been reviewed.[6–8]

Soon after, related autoionization processes were discovered in which the initial vacancy is filled by an electron from a neighboring unit. These were termed electron transfer mediated decay (ETMD).[9–12] If the excess energy is transferred to a third unit which is subsequently ionized, the process is called ETMD(3); if the electron donor is ionized once more, the process is called ETMD(2); and if the excess energy is used to ionize the initially ionized unit, the process is called "exchange ICD".[13,14]

We find that both energy and charge transfer induced autoionization play roles in Ar–Xe, and we detail the relevant processes below.

Rare gas clusters are suitable prototype systems for studies of ICD, as they can readily be produced by supersonic expansion through a cooled nozzle. The size of the clusters can be changed by varying the expansion parameters. The formation of heterogeneous rare gas clusters by coexpansion of a gas mixture cannot a priori be taken for granted, but it was experimentally shown for most combinations of two rare gases when suitable mixing ratios and expansion parameters were used (see references throughout this article).

The first experiments on ICD in heterogeneous systems used Ne–Ar clusters.[15] Those were followed by studies of ICD-like inner-shell decays in aqueous solution.[16–18] Pioneering work also showed the potential for studies of the interface between a substrate and an adsorbate by ICD.[19] More detailed work on Ne–Ar clusters was recently presented by some of the current authors,[20] showing that an analysis of the ICD spectra allowed to decide between structural alternatives for which the photoelectron data were indiscriminate. For this system, a detailed account of the photoelectron spectra with respect to structural features of the mixed clusters is also available.[21]

Several experimental techniques have been used for the study of mixed Ar–Xe clusters, most notably fluorescence spectroscopy, electron diffraction, and photoelectron spectroscopy. Early work focused on the fluorescence of a single Xe atom embedded in an Ar cluster.[22] Increasing the Xe concentration in the expansion led to the formation of Xe_2 and larger Xe complexes inside the clusters.[23] With increasing Xe content, the formation of Xe core–Ar shell systems with a sharp interface between the two species was shown in photoionization experiments.[24,25] This finding was confirmed by electron diffraction.[26,27] Always, the observed Xe content in the clusters

is higher than the Xe content in the expanding gas mixture, as Xe can be condensed much more easily than Ar.[25,27] More recently, photoelectron spectra of small Ar–Xe clusters were analyzed, adding to the findings in earlier work.[28] We will discuss that paper in connection with our results below. For completeness, we mention that Ar–Xe complexes can also be produced by passing clusters from a neat Ar expansion through a zone filled with Xe gas ("pick-up").[29] Clusters produced in such a way can be structurally quite different from those produced by coexpansion.[30]

A number of theoretical works on Ar–Xe clusters aimed at the prediction of minimum energy structures. Most recently, these converged to structures which have the Xe atoms mainly in the interior.[31] Xe was also found to diffuse into the interior of Ar clusters in molecular dynamics simulations after pick-up.[32] The electronic energy levels of very small Ar–Xe clusters were calculated in ref 33, and the secondary electron spectra were simulated for model structures of one argon atom placed on a xenon surface.[34] Interestingly, it was found that Ar $3s^{-1}$ is stable against autoionization in an ArXe dimer, but is destabilized by addition of further Xe atoms or an Ar solvation shell to the system, thereby allowing for combinations of argon and xenon atoms with larger interatomic distances. Again, we will detail these results in conjunction with our current work.

The outline of our paper is as follows: We first delineate our experimental and theoretical methods. Calculations were done for a number of model structures which were systematically varied, and are described in the following section. After that, we describe and discuss our theoretical results for the auto-ionization spectra of the model clusters. Experimental results are then shown, and possible conclusions from comparing them to the calculations are given. Details about the experimental technique and calculated spectra for a wider range of structures are given as Supporting Information.

■ EXPERIMENTAL SECTION

The apparatus used for the experiments consists of a supersonic molecular jet with a cooled nozzle and a magnetic bottle spectrometer, which detects photoelectrons and secondary electrons produced after ionization with synchrotron radiation.[36] A comprehensive description can be found in ref 36, and here we focus on details specific for the current experiment. Commercially obtained Ar and Xe gas was filled into separate cylinders up to pressures suitable for producing a certain mixing ratio. The gases were then allowed to mix before the expansion. Expansion parameters are given in Table 1. Similar expansion conditions are further referred to by the labels "S"–"XL", as given in the table.

Prediction of the sizes of clusters from a supersonic expansion mainly rests on empirical scaling laws,[35] which have been the subject of some discussion. Moreover, such scaling laws originally were derived only for pure gas expansions. A recent investigation of cluster sizes in a mixed Ar–Kr expansion yielded a revised scaling law, which essentially amounts to the use of a weighted average over the atom-specific parameters of the two gases.[37] Although the analogy to our case is not complete, as phase segregation occurs in Ar–Kr to a much lesser extent,[32,38] we expect scaling law cluster sizes between the values calculated for Ar and Xe. Recent analyses of photoionization spectra suggest that mean sizes arrived at by scaling laws are smaller than the actual size, at least for rare gas clusters in the range $\langle N \rangle < 1000$.[39–41] For the expansion

Table 1. Expansion Parameters Used for Cluster Production[a]

	size label	Xe_{in} (%)	T (K)	p (bar)	$\langle N_{Ar} \rangle$	$\langle N_{Xe} \rangle$
Ar	(1)		96.5	0.35	44	
Ar	(2)		96.5	0.67	200	
ArXe	"S"	1.2	174	0.32	4	74
ArXe	"M"	1.2	174	0.49	11	199
ArXe	"L"	1.2	174	0.68	23	431
ArXe	"S"	3.0	172	0.28	3	57
ArXe	"M"	3.0	172	0.51	12	233
ArXe	"L"	3.0	172	0.68	24	458
ArXe	"S"	5.0	167	0.37	7	129
ArXe	"M"	5.0	171	0.51	13	240
ArXe	"L"	5.0	167	0.68	28	537
ArXe	"XL"	2.5	154	2.12	995	18800
Xe		100	183.5	0.68		615

[a]Here, Xe_{in} is the molar fraction of Xe in the gas mixture before the expansion, T is the nozzle temperature, and p is the stagnation pressure. Experiments were performed with $d = 80\ \mu m$ (sizes "S"−"L") and $d = 100\ \mu m$ (size "XL") conical nozzles of 15° half opening angle. We basically have an Ar-seeded expansion of Xe gas, as the freezing point of Ar is much lower. $\langle N_{Ar} \rangle$ and $\langle N_{Xe} \rangle$ refer to cluster sizes for a pure Ar or pure Xe expansion, respectively, at the given conditions, calculated from a scaling law.[35] Inaccuracies in the calculation of $\langle N \rangle$ due to fluctuations of the input parameters are less than 6%; this figure does not include systematic errors of the empirical model.

conditions labeled "S"−"L", we therefore expect that the scaling law estimates are a lower boundary for the actual cluster size.

The expansion chamber for the supersonic jet is separated from the interaction chamber by a non-magnetic, conical skimmer with an opening of 1 mm in diameter (Beam Dynamics). At few cm distance behind the skimmer, the cluster jet was crossed by synchrotron radiation from the BESSY electron storage ring at Helmholtz-Zentrum Berlin. Electrons were detected by a short "magnetic bottle" time-of-flight spectrometer that has been described earlier.[42] Due to its large collection angle, this instrument is particularly suited for experiments that employ electron−electron coincidence detection. Data were recorded in two different beamtimes at the UE112-PGM-1 beamline (sizes "S"−"L" in Table 1) and at the TGM-4 beamline (size "XL" in Table 1). Linearly, horizontally polarized radiation was used. The storage ring was operated in single bunch conditions. Spectra of pure Ar clusters shown for comparison are from ref 41, and a spectrum of pure Xe clusters was recorded with the setup described in ref 40.

The entrance aperture and drift tube of the magnetic bottle spectrometer can be independently biased to influence the electron flight times. For the data shown here, slightly positive bias voltages were used (+1.8 to +2.2 V) in order to have all electrons arriving at the detector within one BESSY single bunch period (800 ns). The detection efficiency was determined as 0.6, with the method outlined in ref 42. Data were converted from flight times to kinetic energy by measuring calibration data for atomic photolines of known binding energy. The systematical uncertainty of this procedure

may lead to a common shift of all experimental kinetic energy data shown in this Article of up to 30 meV.

The high detection efficiency of the instrument is a prerequisite for measuring two-electron emission processes, such as photoelectron emission followed by ICD or ETMD, by using electron−electron coincidence detection. This allows us to filter the full electron spectrum for contributions arising after emission of an Ar 3s photoelectron. ICD/ETMD spectra presented here are based on this method, which has been explained earlier.[42,43] Technical details and full electron−electron coincidence spectra are given in the Supporting Information.

■ THEORETICAL APPROACH

Experimental coincidence spectra are given by the multitude of kinetic energies E_{sec} of the secondary electron and the intensities of the peaks. The latter are proportional to the probability of the decay $P = \Gamma t/\hbar$ as well as the theoretically determinable decay width $\Gamma = \hbar/\tau$, which is inversely proportional to the lifetime τ of the decay process. The manifold of the secondary energies and decay widths will therefore compose the electron−electron coincidence spectrum. In the case of noble gas clusters with given geometrical structures, three aspects have to be taken into account: different decay mechanisms, the possibility to decay with multiple interaction partners, and different decay channels β within each decay mechanism. At the current stage of development, we need to neglect the nuclear dynamics which might additionally play an important role.

This means, for the evaluation of the decay width, we are dealing with a sum over three different indices. For a given structure, it is most convenient to start with a decomposition of the system into interaction partners of the different relevant decay mechanisms, i.e., pairs (combination of two atoms regardless of their internuclear distance) for the ICD and triples (combinations of three atoms) for the ETMD(3). These atoms do not necessarily need to form bonds between each other or even be close, but they are characterized according to fixed internal coordinates. Each pair and each triple leads to a decay spectrum that can be described by the energy of the secondary electron and the decay width, which is, to a first order of approximation, independent of other atoms present in the cluster. In the following, this approach will be called the model of pairs and triples.

In order to determine whether a channel β for a given geometry and decay mechanism is open, i.e., whether it is in accordance with energy conservation, knowledge of the energies of the initial and the final states, E_{in} and E_{fin}, of the corresponding processes is necessary. If the channel is open, the excess energy is carried away by the emitted electron in the form of its kinetic energy, E_{sec}. These energies in the model of pairs and triples can be approximated by

$$E_{in} = SIP(X_{in}) \tag{1}$$

$$E_{fin}^{\beta} = SIP(X_D^{\beta}) + SIP(X_E^{\beta}) + \frac{1}{d} \tag{2}$$

$$E_{sec}^{\beta} = E_{in}^{\beta} - E_{fin}^{\beta} \tag{3}$$

where X_{in} denotes the initially ionized atom and X_D and X_E describe the electron-donating atom and electron-emitting atom, respectively. β denotes the decay channel, characterized by the quantum numbers of the ionized atoms in the pairs and

triples, $\text{SIP}(X^\beta)$ the single ionization potential of vacancy β in atom X, and d the interatomic distance between the atoms X_D and X_E. Atomic units are used. The initially ionized atom X_{in} can coincide with one or both of the final state atoms X_D and X_E. The distribution of the vacancies over the different atoms determines the kind of electronic decay process at hand. Hence, in an Auger process all three atoms coincide, for an ICD process X_{in} coincides with X_D, for an ETMD(2) process X_D and X_E coincide, and for an ETMD(3) process all ionized states are located on different atoms.

The electron emitted by autoionization has the kinetic energy E_{sec}. If the calculated value of E_{sec} is negative, then the final state energy is higher than the initial state energy, and the process is energetically not accessible. Hence, the corresponding channel is closed, as shown in Figure 1 for the Ar $3p^{-1}$Xe $5p_{1/2}^{-1}$ final state. Related to the opening of each channel is an internuclear distance which we will call *channel opening distance* in the following.
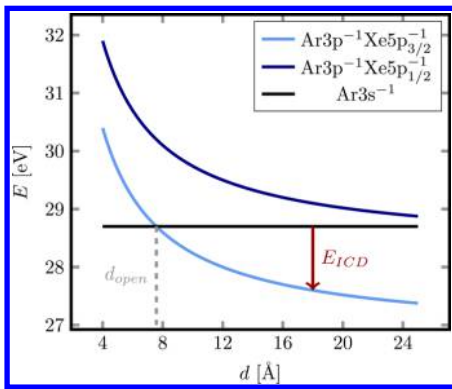
Figure 1. Illustration of channel opening: initial (Ar $3s^{-1}$) and final state (Ar $3p^{-1}$ Xe $5p_{3/2}^{-1}$ and Ar $3p^{-1}$ Xe $5p_{1/2}^{-1}$) energies for ICD in ArXe pairs as a function of internuclear distance, using eq 2 and the experimental ionization potentials given in Table 3. When the final state energy is lower than the initial state energy, the corresponding channel is open. We call the distance at which the energies are equal the "channel opening distance". If the curves do not cross, the corresponding channel is closed.

This ad hoc approach allows us to easily correct for energetic shifts of ionization potentials as observed in larger clusters by adding experimentally or theoretically determined energy shifts $\Delta E(X_I^\beta)$ for a given vacancy I ($=$ in, D, E) and channel β. This yields the working expression for the kinetic energy of the secondary electron:

$$E_{sec}^\beta = \text{SIP}(X_{in}) + \Delta E(X_{in}) - \text{SIP}(X_D^\beta) - \Delta E(X_D^\beta)$$
$$- \text{SIP}(X_E^\beta) - \Delta E(X_E^\beta) - \frac{1}{d} \quad (4)$$

The total decay width Γ is given by the sum over the decay widths of all decay mechanisms. In the case of the ArXe clusters, we only consider ICD and ETMD(3), because the ETMD(2) pathway is energetically not accessible:

$$\Gamma = \Gamma_{ICD} + \Gamma_{ETMD} \quad (5)$$

These are given by the sum over the decay widths of all geometrically different pairs i for the ICD and all geometrically different triples j for the ETMD(3), respectively, and over all channels β:

$$\Gamma_{ICD} = \sum_{i,\beta} N_{ICD,i} \Gamma_{ICD,i,\beta} \quad (6)$$

$$\Gamma_{ETMD} = \sum_{j,\beta} N_{ETMD,j} \Gamma_{ETMD,j,\beta} \quad (7)$$

Here, $N_{ICD,i}$ and $N_{ETMD,j}$ denote the numbers of geometrically equal pairs and triples in a given cluster structure. The total number of pairs reads $N_{ICD} = N_{in}N_{D/E} = N_{Ar}N_{Xe} = \sum_i N_{ICD,i}$, and the number of triples is $N_{ETMD} = N_{in}N_{D/E}(N_{D/E} - 1) = N_{Ar}N_{Xe}(N_{Xe} - 1) = \sum_j N_{ETMD,j}$. The numbers of geometrically equivalent pairs $N_{ICD,i}$ and triples $N_{ETMD,j}$ strongly depend on the structure of the cluster. From these relationships, it can be seen that a higher xenon content in the cluster statistically favors ETMD(3) over ICD.

In previous work,[34,44] we have shown that the decay width for a single pair or triple for a distinct channel β following Wentzel,[45] Feshbach,[46,47] and Fano[48] reads

$$\Gamma_\beta(E_{res}) = 2\pi |\langle \Phi_{in}|\hat{V}|\chi_\beta\rangle|^2 \quad (8)$$

where $|\Phi_{in}\rangle$ and $|\chi_\beta\rangle$ are the initial and final states, respectively, and $\hat{V}$ is the interaction operator between the two, which can be approximated by its asymptotic behavior. For the ICD the approximation reads

$$\Gamma_{ICD,i,\beta} = (2J_{in} + 1) \times$$
$$\frac{3c^4}{8\pi} \sum_{M'_{in}} \left| \begin{pmatrix} J'_A & 1 & J_A \\ -M'_A & M'_A - M_A & M_A \end{pmatrix} \right|^2 \frac{\sigma^{(X_E)}(\omega_{vp,\beta})}{R_i^6 \omega_{vp,\beta}^4 \tau_{in,\beta}} \quad (9)$$

where J_A, J'_A and M_A, M'_A denote the total angular momentum of the initially ionized atom (which is the same as the electron donor atom) in the initial and final states, respectively, which otherwise depend on intrinsic atomic properties which can be determined experimentally, like the ionization cross sections $\sigma^{(X_E)}(\omega_{vp,\beta})$, the radiative lifetimes of the initially ionized state $\tau_{in,\beta}$, and the excess energy transferred to the emitting atom (the energy of the virtual photon) $\omega_{vp,\beta}$.

For the ETMD(3) the approximation reads

$$\Gamma_{ETMD,j,\beta} =$$
$$\frac{c}{\pi} \sum_{m,M_{in,D'}} \frac{\Theta_{m,k}(\alpha_j)\sigma^{(X_E)}(\omega_{vp,\beta}) \left| \langle \tilde{D}_{m,j,\beta}(M_{in,D'}) \rangle \right|^2}{R_j^6 \omega_{vp,\beta}} \quad (10)$$

$$= \frac{c}{\pi R_j^6} \sum_{M_{in,D'}} \left[\left| \langle \tilde{D}_{x,j,\beta}(M_{in,D'}) \rangle \right|^2 (2 + \sin^2 \alpha_j) + \right.$$
$$\left. \left| \langle \tilde{D}_{z,j,\beta}(M_{in,D'}) \rangle \right|^2 (1 + \cos^2 \alpha_j) \right] \frac{c\sigma^{(X_E)}(\omega_{vp,\beta})}{\omega_{vp,\beta}} \quad (11)$$

where $\tilde{D}_{m,j,\beta}$ are calculated transition dipole moments and $\Theta_m(\alpha_j)$ is a function depending on the angle α_j of the triple and the direction of the dipole transition moment m (compare ref 34).

The decay width for the total system is, in the end, normalized to the decay width per initially ionized atom since we are interested in the events after one ionization which could be located at any of the atoms of the corresponding atom type. We thereby yield an averaged decay width for the cluster structure. This step allows the comparison of the total average

Table 2. Structural and Calculated Properties of Some Model Clusters[a]

#	no. of Xe	no. of Ar	% Xe$_{cl}$	structure class	position	relative position	ICD	ETMD	% ICD	related Figure
1	1	12	7.7	cs			0.000	0.000		
2	1	54	1.8	cs			0.000	0.000		7
3	2	53	3.6	cs			0.033	0.167	16.7	7
4	1415	642	68.8	cs			7.039	2.573	73.2	SI
5	561	3310	14.5	cs, icosahedral			1.654	0.256	86.6	8
6	561	3310	14.5	cs, cuboctahedral			1.723	0.355	82.9	8
7	1	13	7.1	cs	surface		0.792	0.000	100.0	4
8	1	13	7.1	cs	edge		0.013	0.000	100.0	
9	1	13	7.1	cs	vertex		0.050	0.000	100.0	
10	2	13	13.3	cs		closest	0.101	0.151	40.1	5
11	2	13	13.3	cs		middle	0.159	0.008	95.4	5
12	2	13	13.3	cs		farthest	0.159	0.002	98.9	5
13	1	55	1.8	cs	surface		0.064	0.000	100.0	4
14	1	55	1.8	cs	edge		0.048	0.000	100.0	
15	1	55	1.8	cs	vertex		0.027	0.000	100.0	
16	1	54	1.8	in	edge		0.077	0.000	100.0	
17	1	54	1.8	in	vertex		0.053	0.000	100.0	
18	2	53	3.6	in			0.117	0.055	68.1	
19	6	49	10.9	in			0.375	0.405	48.1	6
20	6	49	10.9	mixed			0.292	0.674	30.3	6
21	2	36	5.3	cs			0.117	0.151	43.6	SI
22	4	34	10.5	mixed			0.248	0.587	29.7	SI
23	5	33	13.2	mixed			0.335	0.844	28.4	SI
24	13	25	34.2	mixed			0.828	5.414	13.3	SI
25	24	14	63.2	mixed			1.488	16.718	8.2	SI
26	25	13	65.8	in			1.432	4.995	22.3	SI
27	35	3	92.1	in			2.017	7.051	22.2	SI

[a]The cluster structures are characterized by their respective numbers of Ar and Xe atoms, and are arranged in three groups according to gross structural properties. The first group (#1−6) contains Xe core−Ar shell systems of various sizes and relative Xe contents. In the second group (#7−20), model structures for small clusters are displayed, in which 1−2 Xe atoms are added at systematically varied locations to an icosahedral Ar cluster consisting of one or two full shells, or in which 1−6 Ar atoms of such a cluster were replaced by Xe atoms. The last group (#21−27) contains data for calculated minimal energy structures of mixed ArXe clusters.[31] The cluster structures are classified as core−shell structures (cs), structures with segregated xenon atoms (in), and completely mixed structures. The columns "ICD" and "ETMD" are the respective partial decay widths in 10^{-4} eV, and "% ICD" gives the percentage of ICD in the total decay width. See text for details.

decay widths between cluster structures of different sizes and compositions.

In this work we evaluate the secondary energies and decay widths with the program HARDRoC[20,49] using the experimental ionization energies of Table 3 (below) and data from the literature given in Tables II and III of ref 34.

■ CLUSTER STRUCTURES

From the experimental results, we can obtain two hints about the cluster structure: the minimum size and the xenon content. In the following we will use these to construct representative cluster structures, for which we will simulate the ICD and ETMD spectra. At this point we put in a variety of structures in order to learn about general structure−spectrum relationships, therefore making it possible to exclude some of them by comparison of the ICD and ETMD spectra to the experimental ones.

In our previous study,[34] the ArXe clusters were assumed to be large, having more than 1500 atoms. The model structures assumed an fcc structure and not an icosahedral structure, which is energetically favored for small clusters. Most estimated cluster sizes given in Table 1 are much smaller. We use the estimated number of atoms for a pure Ar expansion as the

lower limit for the actual cluster size and start our search for model structures from there. For the smaller clusters measured, these expectation values range from 3 to 21 Ar atoms. The cluster sizes for expansion of a mixed gas are unknown, but for xenon as the second component, a larger size is expected compared to a pure argon expansion, due to the higher polarizability and hence larger cohesive energy of xenon. All clusters contributing to the coincidence spectrum contain at least one xenon atom, as otherwise decay by ICD or ETMD is energetically not allowed.

In a gas expansion, a range of cluster sizes with different structures is produced. However, for small rare gas clusters consisting of less than approximately 1000 atoms, so-called *islands of stability* were found.[50] In mass spectra, clusters with mass numbers corresponding to icosahedral shapes had an abundance that was (slightly) enhanced over other sizes. We therefore started from icosahedral structures and constructed mixed cluster structures by substituting individual atoms with one or the other kind (Ar or Xe), or adding individual atoms close to the desired position within a given structure. After that, the cluster structures were optimized using the unified force field implemented in the Avogadro program (version 1.1.0)[51,52] to give local minimum structures. The method was chosen due to its low computational cost, the possibility to find the next

local minimum structure based on the chosen starting point, and the necessary effort to produce reliable results with density functional theory (DFT) for van der Waals interactions, since in this work we discuss structural trends and not absolute structures. All cluster structures are listed in Table 2.

As discussed in the Introduction, the small clusters will likely deviate from a core–shell structure with a xenon core surrounded by argon shells, as observed for large clusters.[24,32] We therefore start from argon clusters of 13 or 55 atoms, and modify them in one of the following ways:

- add one xenon atom on top of a surface/edge/vertex of the argon core, with an example shown in Figure 2a (one additional xenon atom on top of a surface of a 55-atom argon core) (Table 2, #7–9, #13–15)
- substitute one argon atom in a surface/edge/vertex position (Table 2, #16 and #17)
- substitute one or two argon atoms in the core of the argon cluster by xenon atom(s) for the simulation of the core–shell structures (Table 2, #1–3)
- add two xenon atoms on top of surfaces of a 13-atom argon core in different relative positions (see Figure 3), in order to achieve a xenon content in the cluster close to the measured one (see below) (Table 2, #10–12)
- substitute six argon atoms of a 55-atom argon cluster by xenon atoms, either grouping them or distributing them throughout the cluster (see Figure 2b,c), in order to achieve a xenon content in the cluster close to the measured one (Table 2, #19 and #20)
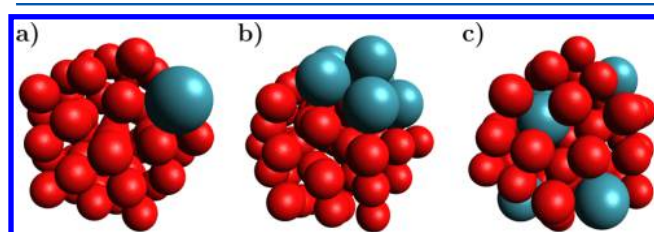
Figure 2. Cluster structures derived from a 55-atom icosahedral structure: (a) one xenon atom on the surface, (b) six xenon atoms inside a 55-atom cluster, grouped on one side, and (c) six xenon atoms distributed randomly in a 55-atom cluster. They refer to #13, #19, and #20 in Table 2.
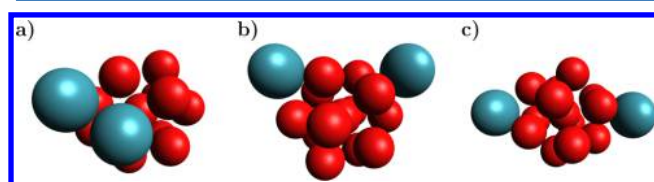

Figure 3. Cluster structures composed of 13 argon atoms and two additional xenon atoms on different surfaces of the argon icosahedron, varying in Xe–Xe distance: (a) closest possible, (b) middle, and (c) farthest away. They refer to #10–12 in Table 2.

These structures were then optimized using force field methods. Furthermore, for comparison with the largest measured ArXe clusters, we constructed also larger core–shell structures (Table 2, #4–6). These were idealized icosahedral and cuboctahedral structures based on the van der Waals radii of argon and xenon, $r_{Ar} = 1.88$ Å[53] and $r_{Xe} = 2.16$ Å.[54]

■ THEORETICAL RESULTS

The geometrical properties as well as the total ICD and ETMD decay widths of the investigated structures are shown in Table 2. It is important to remember that the first ICD channel opens at a channel opening distance of 7.58 Å. In the smallest clusters, with only one argon layer around each xenon atom, the Ar–Xe pair distances are below that value; therefore, no ICD can take place. Also, by definition, two Xe atoms are required for ETMD(3); hence, it cannot occur in clusters with only one xenon atom.

We will now discuss features of several structures, using selected examples. First we consider clusters having an argon core of 13 or 55 atoms plus a single xenon atom on one of the surfaces (see Figure 2a for the structure of clusters with the 55-atom core). Secondary electron spectra simulated for these systems are shown in Figure 4, top panel.
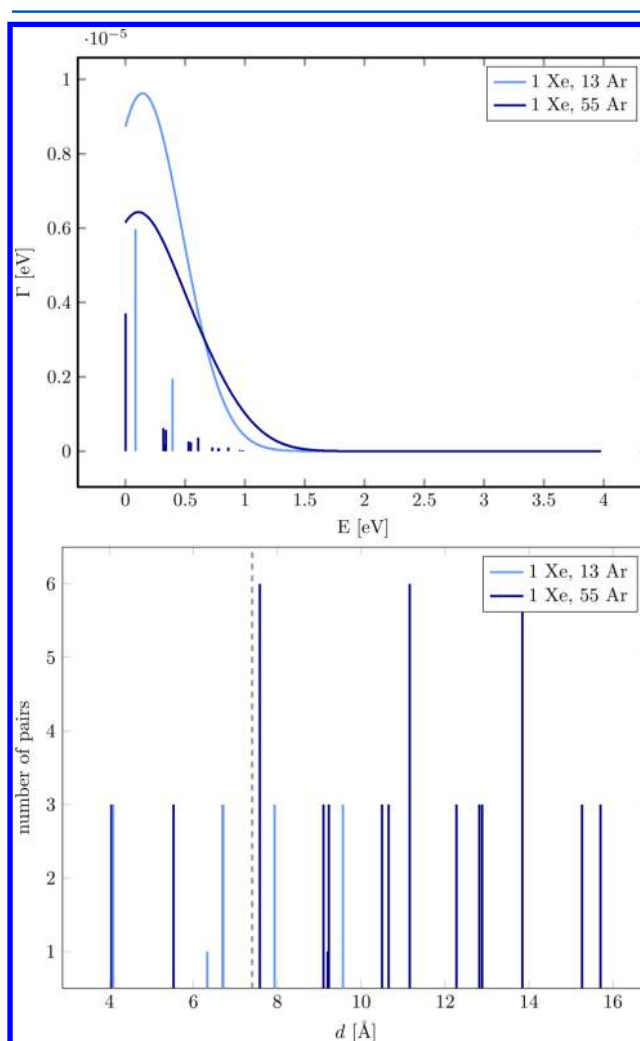
Figure 4. Top panel: Simulated electron emission spectra of an Ar 3s vacancy in argon clusters consisting of 13 and 55 atoms, with an additional xenon atom residing on top of one of the argon surfaces. Bottom panel: Distribution of Ar–Xe distances d in the studied ArXe clusters. The ICD channels to final states involving Xe $5p_{3/2}^{-1}$ and $5p_{1/2}^{-1}$ vacancies open at 7.58 and 36.00 Å, respectively; the former distance is marked by a vertical dotted line. Only pairs at longer interatomic distances contribute to the electron emission spectra. Larger Ar–Xe distances, as found in the larger cluster, correspond to features at a higher kinetic energy of the ICD electron (top panel).

Because the structures contain only one xenon atom, ETMD(3) is not possible; only ICD is expected. The spectrum pertaining to the clusters with larger (55 atoms) Ar core shows signals at higher energies of the secondary electron. These features can be explained by investigating the Ar−Xe distance distributions in the clusters, shown in the lower panel of Figure 4. Every different value of the atom pair distance results in a different energy of the secondary electron, and only pairs with a distance larger than the channel opening distance (dashed gray line) will contribute to the spectrum. In our model, there is a one-to-one correspondence between interatomic distance d and kinetic energy of the ICD electron: the larger the interatomic distance, the higher is the kinetic energy of the secondary electron for a given channel. Therefore, the spectrum of the cluster with a 55-atom core extends to higher energies. This relation between ICD energy and cluster size holds true for all cluster structures.

For clusters with more than one xenon atom, ETMD(3) is also possible. Depending on the positions of the xenon atoms relative to each other and to the Ar core, the spectra are expected to be different. As an example, we discuss clusters with a core of 13 argon atoms and two xenon atoms on different surfaces. Their xenon content is 13.3%, and thus close to the experimental value of 10−12% for the lowest xenon admixture. The cluster structures were illustrated in Figure 3, and simulated spectra are shown in Figure 5. In all three cases,
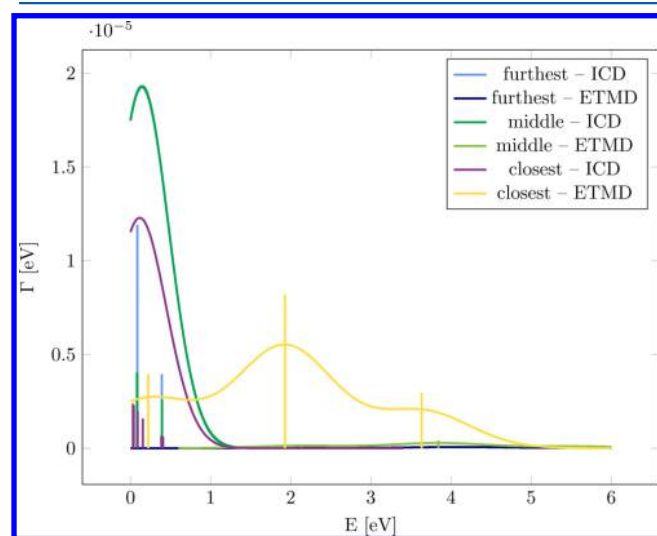

Figure 5. Simulated electron emission spectra of an Ar 3s vacancy in argon clusters consisting of 13 argon atoms with two additional xenon atoms on top of two different argon surfaces. ICD and ETMD spectra are shown for three different relative positions of the two xenon atoms. The ICD spectra for the farthest and middle relative position coincide. If the xenon atoms are close to each other, an ETMD process is clearly visible. In the other two cases, the spectra are dominated by the ICD spectrum.

both ICD and ETMD(3) are energetically allowed. The ICD spectra do not change qualitatively when the second xenon is added. However, the ETMD(3) spectra are very sensitive to the relative positions of the two xenon atoms. Two aspects have to be taken into account: an energy shift of the peaks due to different charge distances d in the final state (i.e., the interatomic Xe−Xe distance) and the decrease of the decay width with R^{-6}, R being the distance between the electron transfer unit and the xenon atom ionized in the final state. The

larger the distance between the xenon atoms, the higher are the energies of the secondary electrons. For the case of xenon atoms on argon surfaces, this at the same time means a larger distance between the Ar−Xe pair involved in the electron transfer and the electron emitting xenon atom; hence, the decay widths are smaller. Therefore, a significant contribution from ETMD(3) compared to ICD is seen only if the two xenon atoms reside on two adjacent surfaces. The three energetically separated peaks in the ETMD(3) spectrum pertain to different combinations of the Xe $5p_j^{-1}$ vacancy states, which have a substantial fine-structure splitting (compare to Figure 6).

For the 55-atom clusters, a xenon content of 10−12% corresponds to six xenon atoms out of a total of 55 atoms. These can form a connected group in one part of the cluster or can be evenly distributed, as shown in Figure 2b,c. The ICD and ETMD(3) spectra for these structures are shown in Figure 6.
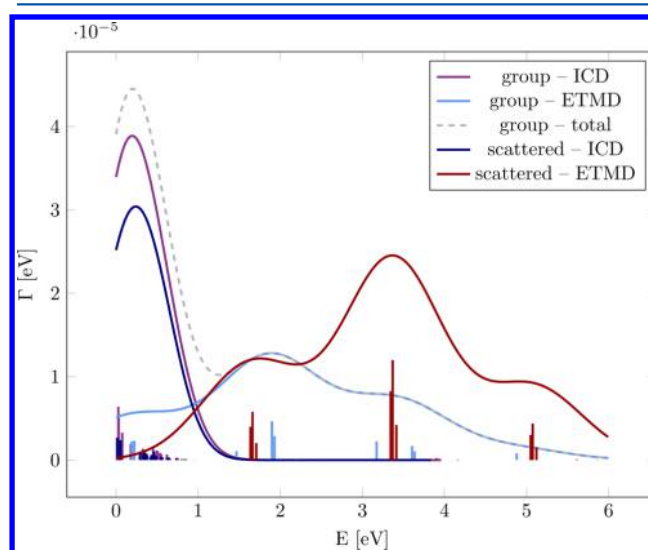
Figure 6. Same as Figure 5, for clusters consisting of 55 atoms, six of which are xenon atoms. These are either grouped on one side of the cluster (label "group") or evenly distributed in the cluster interior (label "scattered").

For both cases, the overall ICD spectra are very similar and show a maximum at a kinetic energy of approximately 0.3 eV. In the case of grouped xenon atoms, the ICD spectrum extends to slightly higher energies, corresponding to ArXe pairs at slightly larger spatial distances. A more significant difference is observed in the ETMD(3) spectra. The interatomic xenon distance is shorter in clusters, in which the xenon atoms form a connected group. Hence, the triple structure of the ETMD(3) spectrum is seen at lower kinetic energies. Additionally, the probability for electron transfer from a xenon to an argon atom decreases exponentially with the interatomic distance. Therefore, only those xenon atoms which have direct argon atom neighbors make a significant contribution to the total decay width, and the total ETMD(3) decay width is lower for the structure with grouped xenon atoms than for the structure with evenly distributed xenon atoms (see Table 2).

For comparison with the previous assumptions of a xenon core surrounded by argon atoms, we investigated clusters of 13 and 55 atoms with one or two xenon atoms in the core. Some of the corresponding spectra are shown in Figure 7.
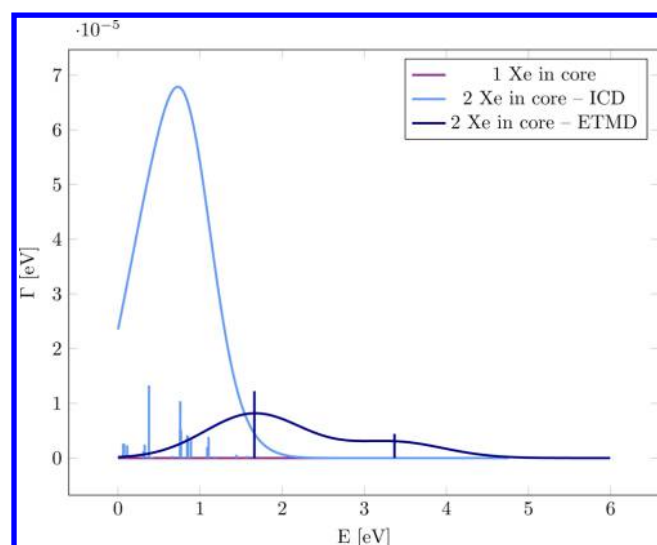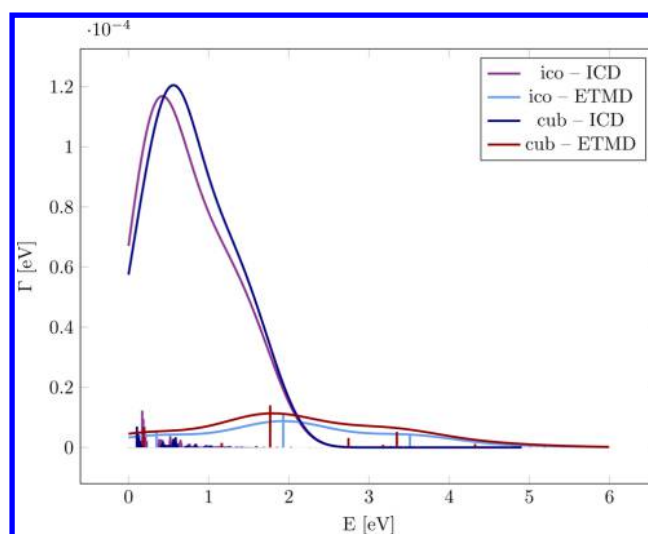
Figure 7. Same as Figure 5, for argon clusters with one or two xenon atoms in the core of the cluster (55 atoms total). All ICD and ETMD channels are closed if the cluster contains only a single xenon atom. For clusters with two xenon atoms in the core, the first ICD channel is open for some pairs, and additionally ETMD is possible for multiple triples. Due to a different distance distribution compared to the clusters with an argon core (Figure 5), the ICD peak is shifted to higher kinetic energies.

Figure 8. Same as Figure 5, for a large cluster consisting of a xenon core of 561 atoms surrounded by five complete layers of argon atoms (Xe content, 14.5%) for both an icosahedral and a cuboctahedral basic structure. The ICD and ETMD peaks overlap such that the ETMD peak is unlikely to be visible.

For a core consisting of two xenon atoms, both an ICD spectrum and an ETMD(3) spectrum can be seen. Compared to the cluster structures involving an argon core, the ICD peak is shifted to higher ICD electron energies. Additionally, the ICD and ETMD(3) spectra overlap. For ETMD(3), only three of the four different decay channels are energetically allowed.

In the first experiments, very large argon–xenon clusters of ∼4380 atoms with a xenon content of 19% were measured,[55] which we approximate in one example by a cluster consisting of 561 xenon atoms surrounded by five layers of argon atoms (3871 atoms in total). In order to take the better stabilization of charges in larger clusters into account, the ionization energies of the XL clusters (see Table 3) were used. The spectra are shown in Figure 8.

Compared to the small clusters with a xenon core in Figure 7, the ICD peak is broadened and shifted to higher ICD electron energies, which is expected due to the larger interatomic Ar–Xe distances in the large cluster and the better stabilization of charges, which is relevant mostly for the final state, but also for the initial state. The ETMD(3) peak is shifted to slightly higher energies as well. This allows opening of the fourth decay channel, pertaining to Xe $5p_{1/2}^{-1}$ Ar $3p_{1/2}^{-1}$ final states.

We also note that the percentage of decay via ICD is practically independent of the Xe content for large clusters with a Xe core–Ar shell structure. This can be expected, as both decay processes are most pronounced for the atoms in the interface region of the xenon core and the argon shell. The ETMD(3), depending on the electron transfer from one xenon atom to the initially ionized argon atom, and hence on the corresponding orbital overlap, is purely an interface effect that involves the argon atoms with direct xenon neighbors and the two xenon layers closest to the argon shell. The ICD has a stronger long-range character, due to which the description of decays with partners of size at least twice the smallest channel opening distance is necessary for clusters. However, the bigger the clusters are, the more homogeneous the interface region becomes for clusters of different sizes. This manifests itself in the distribution of relevant Ar–Xe pair distances (compare Figure 4, lower panel). As a consequence, the ICD spectra of two large clusters of different sizes hardly differ.

All these results neglect the effect of nuclear dynamics, which might affect the spectra. Possible reasons are distance-dependent channel closings and openings, a different distribution of interatomic distances due to vibrations, and their different impact on the ICD and the ETMD(3). For example, for the ICD in the neon dimer, the treatment of nuclear dynamics increases the decay width by approximately a factor of 2.[56] However, the atomic displacement can be expected to be far less severe in clusters than in dimers or trimers. Additionally, the elongation of one interatomic distance in a cluster automatically results in the shortening of a different interatomic distance, which will reduce the overall effect. Therefore, there will be a broader spectrum of final state charge distances d, resulting in a broadening of the peak. This was taken into account by folding the stick spectrum with Gaussians with a width of 300 and 600 meV for the ICD and ETMD(3), respectively. While the width of the ICD peaks was estimated from the potential energy surface of the ArXe dimer, the situation is more complex in case of the ETMD(3), with three degrees of freedom involved. It was therefore guessed to be twice the width of the ICD peak.

The channel closing due to shortening of the interatomic distance is not relevant for the ETMD(3) process in the ArXe clusters treated in this work, because this would require unnaturally short interatomic distances. However, for the ICD, it might result in a lower number of pairs with open decay channels and hence a decrease of the decay width. Since the peaks in the convoluted spectrum contain contributions from several atom pairs at different distances, this would result in a small peak shift to higher energies of the combined peak at lowest energy. For a more detailed discussion of nuclear dynamics for the ICD in dimers vs clusters, see ref 57.

Table 3. Properties of the Outer Valence Spectra of Mixed ArXe Clusters[a]

	size label	Xe_{in} (%)	Ar 3p		Xe $5p_{1/2}$	Xe $5p_{3/2}$		Xe_{cl} (%)
			E_b (eV)	w (eV)	E_b (eV)	E_b (eV)	w (eV)	
Ar	(1)		15.3	1.1				
Ar	(2)		15.1	1.3				
ArXe	"S"	1.2	15.36	0.9	13.07	11.75	0.85	12
ArXe	"M"	1.2	15.30	1.0	12.97	11.61	0.85	11
ArXe	"L"	1.2	15.25	1.1	12.91	11.52	1.08	10
ArXe	"S"	3.0	15.39	0.8	13.06	11.68	1.02	29
ArXe	"M"	5.0	15.31	0.6	12.96	11.44	1.24	53
Xe					12.76	11.19	1.18	100
ArXe	"XL"	2.5	15.15	1.3	12.59	11.01	1.24	19
Ar, Xe	(th.)		15.3		13.0	11.5		
	(atomic)[59,60]		15.76 | 15.94		13.43	12.13		

[a]Spectra of pure Ar and Xe clusters are included for reference. All spectra were recorded at $h\nu = 17$ eV, except for the pure Xe clusters ($h\nu = 60$ eV). Binding energies E_b were determined as the center of gravity of the respective feature, while band widths w are the fwhm of a Gaussian fit. The average Xe content of the cluster ensemble, Xe_{cl}, was determined from the areas of the respective photo lines, corrected by their atomic photoionization cross sections (Ar, 33.0 Mb; Xe, 51.3 Mb).[58] Uncertainties are estimated as ±3% for the Xe content and 0.05 eV for the binding energies. The row labeled "(th.)" gives the binding energies used in the simulations of this paper, and the last row shows their atomic counterparts. Values for Ar 3p in the last row refer to the fine structure states.

■ EXPERIMENTAL RESULTS

Outer Valence Spectra. This section describes and discusses the outer valence spectra of the mixed Ar−Xe clusters. The main information we obtain from these spectra within the context of our theoretical considerations are the single ionization potentials and the relative Xe contents in the mixed clusters (see Table 3).

Figure 9 shows the outer valence spectra of small and large ArXe clusters, compared to clusters of the pure gases. Qualitatively similar spectra have been published without detailed discussion in ref 28. Differences are seen in particular for the Ar component. In pure Ar clusters, outer valence photoionization leads to a broad band, caused by both spin−orbit coupling and crystal field splitting. A distinction between the Ar $3p_{1/2}$ and the Ar $3p_{3/2}$ derived cluster bands therefore cannot be made. The relative importance of these two mechanisms remains under debate.[40,61,62] For larger clusters (e.g., $\langle N \rangle = 190$, black trace), the maximum at low binding energies becomes more pronounced and is identified with emission from the cluster interior.[40,61] At the particular photon energy selected here, atop of this band a sharp feature is also visible (in Figure 9 at a kinetic energy of about 1.8 eV). For larger clusters (above $\langle N \rangle \approx 100$), over a range of photon energies of about 3 eV, its apparrent binding energy changes in a way which is reminiscent to photoemission of crystalline bulk matter ("dispersion").[41,62]

Ar 3p spectra of the smaller mixed clusters (Figure 9c and Figure 10) show neither of these traits. Rather, the Ar band is symmetric, less wide than in the pure clusters, and at a higher binding energy. Even for very large clusters (Figure 9b), the asymmetry of the 3p band and the "dispersing feature" do not appear. We characterize the spectral shape by giving a single value for the Ar 3p binding energy and the full width at half-maximum (fwhm) of the feature. Values for different expansion parameters, and for both Ar and Xe valence lines, are collected in Table 3.

We find experimentally that the clusters we produced have a Xe content, Xe_{cl}, between 10% and 50%. A slight decrease of the binding energy with cluster size is seen for all outer valence
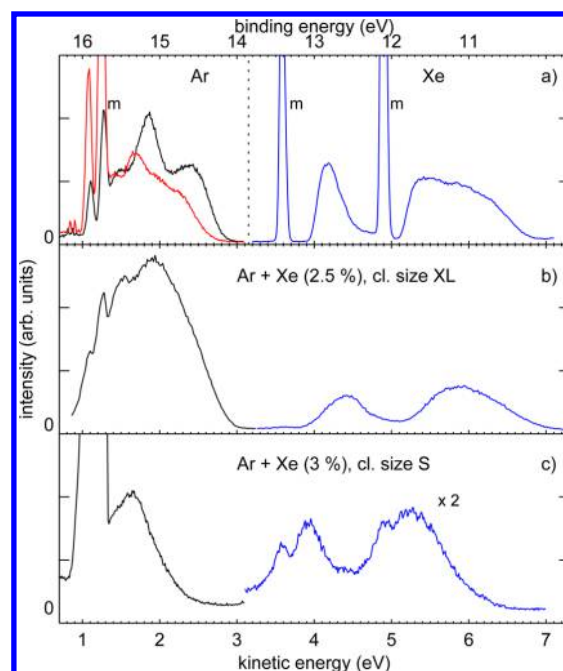
Figure 9. Outer valence photoelectron spectra of mixed Ar−Xe clusters, in comparison to the pure species. Panel (a) shows the outer valence region of homogeneous Ar(1) (red), Ar(2) (black), and Xe clusters (see text and Table 1 for details). Panels (b) and (c) show spectra of the mixed species with different mean sizes. Sharp lines marked "m" (for "monomer") result from photoionization of uncondensed atoms into the Ar $3p_{1/2,3/2}$ and Xe $5p_{1/2,3/2}$ final states. Labels in (b) and (c) give the Xe content in the expanding gas mixture (Xe_{in}), which is lower than the Xe content observed in the heterogeneous clusters (Xe_{cl}). The photon energy was 17 eV, in contrast to the pure Xe cluster spectrum (60 eV).

lines, and is attributed to a larger final state polarization energy in larger clusters.

For further interpretation of the shape of the Ar peaks, we refer to photoemission spectra of condensed Ar monolayers, measured in several settings.[63,64] Spectra were reported for
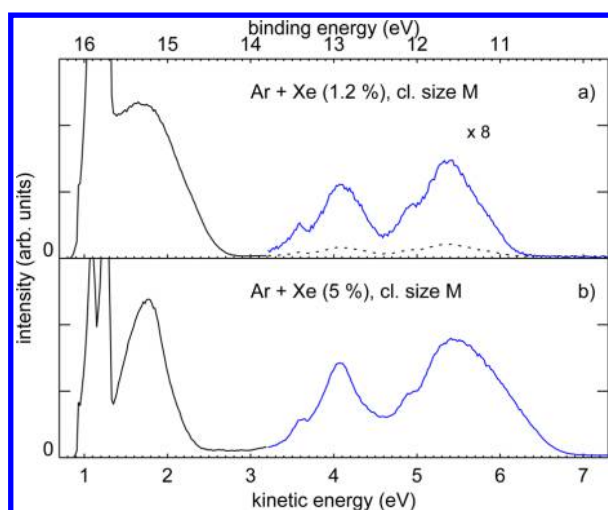
Figure 10. Outer valence photoelectron spectra of mixed Ar−Xe clusters from gas mixtures with different Xe concentrations. For better visibility, a scaling factor is applied to the Xe part of the spectrum in panel (a). The dotted line shows the unscaled spectrum in this region. See Figure 9 and text for details.

physisorption of Ar on two different metal single-crystal substrates, and for Ar atop of a Xe spacer layer adsorbed on the metal. While the binding energy depends on the substrate, the spectral shape is very similar in all cases. Most spectra were recorded for emission along the surface normal and show a double peak split by about 0.5 eV, leading to a structure with a fwhm (w) of about 1 eV. Although the splitting is larger than the gas phase fine structure split of 0.18 eV, the associated states have been assigned to Ar $3p_{1/2}$ and $3p_{3/2}$. A crystal field splitting of the $3p_{3/2}$ state has been assumed to be also present, but with a smaller value of approximately 0.1−0.2 eV.[64] The spectrum clearly changes when going to an emission angle of 40° with respect to the surface normal (Figure 2 in ref 64). The higher binding energy peak significantly loses intensity, and the spectrum is now dominated by a single peak comprising both crystal field split substates of Ar $3p_{3/2}$, with a fwhm (w) of only 0.4 eV. As our measured spectrum is comprised of contributions recorded under all emission angles with respect to the cluster surface, grazing emission will be the rule. We therefore believe that the arguments given above make it plausible that only a single peak is observed in all our spectra.

Emission from the Xe $5p$ state shows a much larger fine structure splitting than that from the Ar $3p$ state; it dominates the spectrum even in clusters (where other broadening mechanisms are also present). The shift of the cluster bands with respect to the monomer lines in the largest mixed clusters we have probed (Figure 9b) are similar to the ones in the pure Xe spectrum, the scaling law size of which is at somewhat more than five filled shells. This indicates an approximate upper limit for the size of the Xe core in our mixed clusters, as their binding energy shift might be somewhat higher than that in pure clusters, due to polarization of covering Ar layers. Xe cluster features in the spectra of mixed clusters appear less asymmetric than in the pure Xe spectrum, and also less asymmetric than in some of the ArXe spectra shown in ref 28. This might be caused by the difference in photon energy ($h\nu$ = 90 eV in ref 28 and for the pure Xe spectrum, $h\nu$ = 32 eV for the mixed ArXe spectra in this work).

In Figure 10, we compare the outer valence spectra of clusters with similar expansion conditions but different

composition of the gas mixture. A Xe-rich mixture obviously leads to clusters with more intense Xe photolines, but besides that the main change is a narrowing of the Ar band. A comparison with the Ar monomer features (clipped in the figure) also shows an increased degree of condensation for the Ar gas in the expansion.

For the smallest clusters we produced, a possible model is provided by calculated minimum energy structures of $Ar_N Xe_{38-N}$ (Figure 7 in ref 31). We there see that, for a Xe content of less than 60%, core−shell systems are *not* formed, and although the Xe atoms tend to connect, the degree of Ar−Xe mixing is large. While for low Xe content (approximately 10%) some Ar atoms have only Ar nearest neighbors, for larger Xe content all Ar atoms seem to see both Ar and Xe nearest neighbors. We believe this leads to the Ar $3p$ narrowing pointed out above. For Figure 10, possibly, some clusters of our ensemble already are in the core−shell regime, which would lead to an even lower $3p$ width.

For the largest clusters we have produced (Figure 9b), the low binding energy of the Xe lines and the broadening of the Ar feature without appearance of the "bulk Ar" maximum support formation of a Xe core covered by at least two layers of Ar. If the scaling law size for a pure Ar expansion is taken as the lower limit for the cluster size, from the observed Xe content we arrive at clusters composed of a Xe core with four layers, covered by three layers of Ar (see Supporting Information).

Finally, comparing Figure 10 to Figure 9 reveals that much larger changes in the valence emission spectra occur as a result of changes in size than changes of the (relative) Xe content. This finding is supported by the spectra shown in ref 28.

Inner Valence Spectra. We now focus on the Ar inner valence ($3s$) vacancy states.

Figure 11 shows the Ar part of the inner valence spectrum for representative ArXe clusters. The total photoelectron signal looks similar to literature spectra for pure Ar clusters.[66,67] A low-energy tail seen for the Ar $3s$ monomer line results from the transmission properties of the electron spectrometer, together with the strongly positive angular distribution parameter of this line.[67,68] The Ar $3s$ cluster line shows no splitting into bulk and surface components, different from literature on pure clusters but in agreement with our discussion of the outer valence spectra. The binding energy of the cluster line has values between 28.85 and 28.70 eV for all cluster ensembles with size labels "S"−"L", and 28.67 eV for the largest clusters measured. A small but systematic decrease of the binding energy is observed when the cluster size is increased. The value assumed in the simulations is 28.7 eV.

If we produce a spectrum only from those electrons recorded as part of a two-electron coincidence (electron pair with kinetic energies (e_1, e_2)) the apparent intensity drops (compare panel b to panel a, and panel d to panel c in Figure 11). This can partly be attributed to the finite detection efficiency of the spectrometer. Moreover, the monomer part of the Ar $3s$ signal completely disappears, as $3s$ photoionization of an uncondensed Ar atom in the gas jet cannot lead to emission of a second electron. Further features of these diagrams and the least-squares fits shown in the Figure are discussed below.

ICD/ETMD Spectra. In Figure 12, we show the spectra of ICD/ETMD electrons pertaining to emission of an Ar $3s$ cluster photoelectron. Due to their low kinetic energy, without use of a coincidence method they could hardly be separated from the background of inelastically scattered photoelectrons.[69] This and the following Figure constitute the central
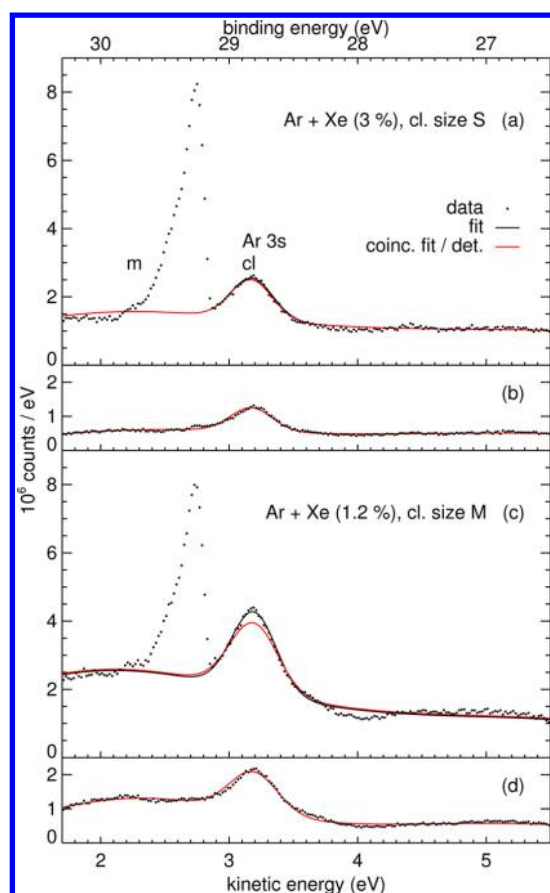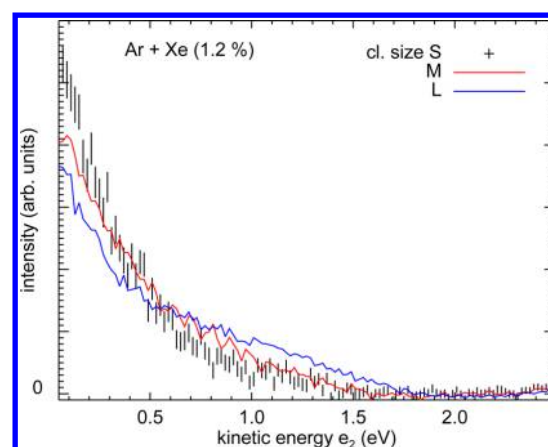
Figure 11. Electron spectra of mixed Ar–Xe clusters after photoionization in the inner valence region. Symbols show the Ar 3s photoline from clusters ("cl") and uncondensed Ar monomers ("m"), atop of a background resulting from inelastic intracluster scattering of outer valence photoelectrons ("excitonic satellites").[65] The photon energy was $h\nu = 32$ eV. Panel (a) shows all electrons accumulated. For the same conditions, in panel (b) we show only electrons that were detected in coincidence with a secondary electron of lower kinetic energy. The black solid trace in (a) and red solid trace in (b) result from a least-squares fit to the cluster part of the spectrum. The red solid trace in (a) is the fit shown in (b), divided by the detection efficiency of the spectrometer of 0.6. Panels (c) and (d) show the same type of data for smaller clusters with a lower Xe content. See text for details.

Figure 12. Energy spectrum of all coincident secondary (ICD or ETMD) electrons of kinetic energy e_2 pertaining to primary electrons of kinetic energy e_1 in the Ar 3s binding energy region. Spectra were recorded with a photon energy of $h\nu = 32$ eV. Black error bars show the data points for the smallest clusters measured ("S"); two larger clusters sizes are shown by the red and blue traces. Error bars for the latter are smaller than the ones shown and have been omitted. For better comparison, all spectra are shown area-normalized.

Figure 13. Energy spectrum of all coincident secondary (ICD or ETMD) electrons, kinetic energy e_2, for clusters of the same size, but from gas mixtures with different Xe concentration. See Figure 12 for details.
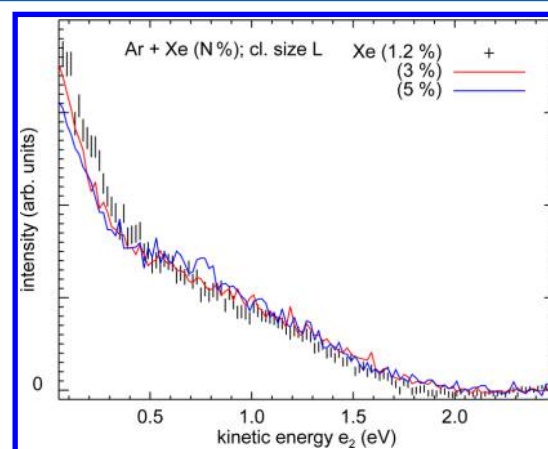
experimental result of the article. Spectra recorded at $h\nu = 34$ eV as a cross-check quantitatively agree to those shown here. This underpins our assignment of this intensity to an autoionization process. Further details on the data acquisition and analysis methodology, as well as the 34 eV spectra, are given in the Supporting Information.

Spectra for the three different cluster sizes in Figure 12 are significantly different: Spectra for the larger clusters acquire more intensity in the 1−1.5 eV region and have less intensity for energies below 0.5 eV. In contrast to that, the ICD/ETMD spectrum hardly varies when the composition of the expanding gas mixture, and with that the relative Xe content of the clusters, is changed (Figure 13). The full set of ICD/ETMD spectra is shown as Supporting Information.

We now discuss which fraction of Ar 3s vacancy states relaxes via either ICD or ETMD. A method to derive this information has been established by some of us.[70] Briefly, we correct the intensity of the Ar 3s photoline in the coincident spectra by the detector efficiency, and divide it by the total (coincident and non-coincident) Ar 3s intensity. The result gives the branching ratio of decay via ICD/ETMD vs the sum of all channels, including those not involving electron emission. (If all Ar 3s vacancies decay by emission of another electron, the coincident and non-coincident count rate differ only by the probability for the spectrometer to actually detect the secondary electron (0.6 for this data set).) To arrive at quantitative results, we have performed least-squares fits of the non-coincident and coincident e_1 spectra. The fits assumed one or two Gaussian peaks, respectively, atop of a background modeled by two more Gaussian curves with very large widths. The peak pertaining to the Ar 3s cluster photoline, with the background added, is shown by the black solid trace in Figure 11a and red solid trace in Figure 11b. Moreover, the line labeled 'c.fit/det.' shows the fit to the coincident events, corrected by the detection efficiency, and plotted atop of the non-coincident intensity. This virtually agrees with the fit to the total spectrum in Figure 11a, but not in 11c. The corresponding figure for the

K

ICD/ETMD efficiency comes out as one for **11a**, and significantly smaller than one for **11c**. Figure 14 shows all
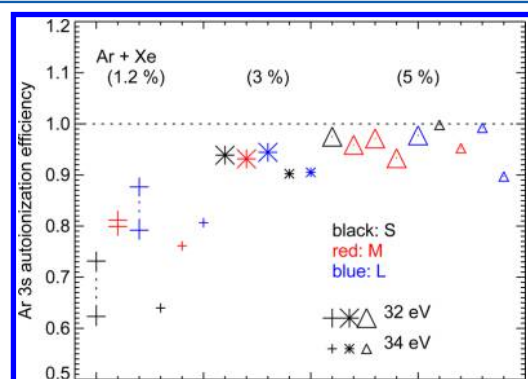
Figure 14. Efficiency of the decay of Ar 3s ionized states in ArXe clusters by emission of a secondary electron via ICD or ETMD. Values are arranged by Xe content of the initial gas mixture ("+" symbols, 1.2%; asterisks, 3%; triangles, 5%). Symbol sizes indicate the photon energy (large symbols, 32 eV; small symbols, 34 eV), and color indicates the cluster size (black symbols, S; red, M; blue, L). See text for details.

results of this analysis. The error in the autoionization efficiency shown is mainly determined by uncertainties in the peak/background separation. For the gas mixture with a Xe_{in} of 1.2%, we therefore show results from fits using two different choices of the background shape in Figure 14. Statistical errors are much smaller than the differences between the pairs of values arrived at such.

We found an Ar 3s autoionization efficiency which is compatible with unity, within the accuracy of our experiment, for all clusters except those with the lowest Xe content (Xe_{cl} approximately 10−12%). For the latter, also a decrease of the efficiency with decreasing cluster size is seen. Two main reasons can be identified that may cause a decrease in autoionization efficiency. First, in small clusters with a low Xe content, for some Ar atoms no Xe partners allowing either ICD or ETMD might be available. A simple example are clusters containing just a single Xe atom. This mechanism would gain in importance for cluster ensembles with small $\langle N \rangle$. Second, if only Xe partners at very large distances are available, ICD might be outpaced by other decay processes, most importantly fluorescence.

■ DISCUSSION

We now interpret our experimental findings in view of the simulated results described in the Theoretical Results section. Figure 14 shows that, for Ar $3s^{-1}$ states, autoionization by either ICD or ETMD is the only mode of relaxation, except for the clusters with the smallest Xe content. We consider this a remarkable result, because ICD of these states is only possible with a Xe atom in the second coordination shell of the decaying Ar vacancy (or shells even farther apart), which significantly slows down the ICD process. Also, decay rates for ETMD were found to be small in early studies of this effect.[9] Nevertheless, even in this situation, the non-local autoionization channels foreclose radiative decay.

Structurally, all experimental ICD/ETMD spectra have a maximum at or near the lowest kinetic energy that could be measured (50 meV), and they decrease in intensity to less than half for kinetic energies already below 1 eV. Qualitatively, this

shape fits to the ICD contributions in the autoionization spectra discussed in the Theoretical Approach section, but not to the ones from ETMD. The calculated ETMD spectra have a typical three-fold structure with peaks between 3.5 and 5 eV, 1.5−2.5 eV, and around 0 eV kinetic energy. The former two features seem not to be present in the experimental spectra. Due to restrictions in the detector electronics, electron pairs with very similar kinetic energy cannot be detected. The highest kinetic energy for an autoionization electron that can be detected in coincidence with a photoelectron of ∼3.5 eV ($h\nu$ = 32 eV) is around 2.5 eV. Very weak intensity is observed at this energy, and also at higher e_2 energies that can be probed at $h\nu$ = 34 eV (Supporting Information).

As a cross-check for our theoretical methods, we have calculated the radiationless decay spectrum of Ar $3s^{-1}$ in ArKr, which may arise *only* from ETMD(3),[12] and arrived at qualitative agreement with the experimental data.[71]

The size-dependent trend within the experimental data is in qualitative agreement to the change in the calculated spectral shape for ICD in systems of increased size (compare Figure 5 to Figures 7 and 8).

We are therefore led to the conclusion that the autoionization spectra we incur are dominated by ICD to nonnearest-neighbor atoms, while the intensity of the ETMD channel is low. We recall the factors that lead to a propensity for decay via one mechanism or the other, which were discussed in the Theoretical Results section. For ETMD to occur with a measurable rate, two Xe atoms have to be present in the vincinity of the decaying Ar atom (Figure 5). Should that be the case for a large part of the Ar atoms in some cluster structure, ETMD can even dominate over ICD (Figure 6 and Supporting Information). Model structures shown in Figures 5 and 6 have a Xe content similar to the lowest one probed in our experiment (∼11%). For a higher Xe content, ETMD will always dominate the spectra if the two species are given the chance to mix, as, e.g., in the calculated minimum energy structures of N = 38 ArXe clusters (Supporting Information). On the other hand, in core−shell systems, decay via ETMD is probable only for Ar atoms in the interface layer, as this mechanism requires some wave function overlap between Ar and one of the Xe atoms involved. For the core−shell systems we have investigated, the likelihood of decay via ETMD stays below 27% even for a Xe content above 50% (Table 2).

In summary, there are two structural motifs that can best be reconciled with our experimental data:

1. small clusters containing only few Xe atoms that are spread out to distant positions on the cluster surface, and
2. systems with a compact Xe core and Ar outer layers.

These structures are compatible with the findings from corelevel photoelectron spectroscopy by Lindblad et al.,[28] who proposed the former structure for the smallest clusters in their study and the latter for larger ones. As even in these two cases intensity for decay via ETMD would not vanish completely, we have to leave it open, though, whether other mechanisms are present which further suppress ETMD vs ICD.

While in early work on ICD, it has been almost a paradigm that the decay involves two *neighboring* atoms or molecules,[6] more recently significant intensity for non-nearest-neighbor ICD has been found also in other systems. One example is Ne−Ar after Ne 2s ionization, where decay to Ar in the second coordination shell is clearly visible, despite the fact that in this system decay involving nearest neighbors is energetically

allowed.[20] A further theoretical delineation of the respective factors has recently been presented by one of us.[57]

SUMMARY

We have presented comprehensive experimental and theoretical data for the autoionization of inner valence ionized states in ArXe clusters. Both ICD and ETMD are allowed for most cases we considered. Because of energetical reasons, ICD requires a separation of the final state vacancies of 7.58 Å or more, which is about two times the typical Ar–Xe distance. We found that autoionization has an efficiency of 0.8–1.0, within the experimental accuracy; that is, it dominates over other modes of relaxation. By comparing our measured spectra to calculations, we identified "long-range" ICD as the most important decay mode and were able to determine the most probable structural motifs to be a xenon core surrounded by several argon layers for large clusters and argon clusters with very few xenon atoms spread out over the surface.

ASSOCIATED CONTENT

⑤ Supporting Information

The Supporting Information is available free of charge on the ACS Publications website at DOI: 10.1021/acs.jpcc.6b06665.

> Detailed experimental approach, results, and theoretical spectra for structures **21**−**27** (PDF)

AUTHOR INFORMATION

Corresponding Authors
*E-mail: uwe.hergenhahn@iom-leipzig.de.
*E-mail: elke.fasshauer@uit.no.

Present Addresses
×M.F.: Institut für Optik and Atomare Physik, Technische Universität Berlin, Hardenbergstr. 36, 10623 Berlin, Germany
#M.M.: Department of Physics and Astronomy, Uppsala University, Box 516, 75120 Uppsala, Sweden
▽T.A.: Center for Free-Electron Laser Science/DESY, Notkestr. 85, D-22607 Hamburg, Germany

Notes
The authors declare no competing financial interest.

ACKNOWLEDGMENTS

REFERENCES

(1) Special issue: Current Trends in Clusters and Nanoparticles. *J. Phys. Chem. C* **2015**, *119*, (20).

(2) Cederbaum, L. S.; Zobeley, J.; Tarantelli, F. Giant Intermolecular Decay and Fragmentation of Clusters. *Phys. Rev. Lett.* **1997**, *79*, 4778–4781.

(3) Slavíček, P.; Winter, B.; Cederbaum, L. S.; Kryzhevoi, N. V. Proton-Transfer Mediated Enhancement of Nonlocal Electronic Relaxation Processes in X-ray Irradiated Liquid Water. *J. Am. Chem. Soc.* **2014**, *136*, 18170–18176.

(4) Marburger, S.; Kugeler, O.; Hergenhahn, U.; Möller, T. Experimental evidence for Interatomic Coulombic Decay in Ne clusters. *Phys. Rev. Lett.* **2003**, *90*, 203401.

(5) Jahnke, T.; Czasch, A.; Schöffler, M. S.; Schössler, S.; Knapp, A.; Käsz, M.; Titze, J.; Wimmer, C.; Kreidi, K.; Grisenti, R. E.; et al. Experimental Observation of Interatomic Coulombic Decay in Neon Dimers. *Phys. Rev. Lett.* **2004**, *93*, 163401.

(6) Hergenhahn, U. Interatomic and intermolecular coulombic decay: The early years. *J. Electron Spectrosc. Relat. Phenom.* **2011**, *184*, 78.

(7) Averbukh, V.; Demekhin, P.; Kolorenc, P.; Scheit, S.; Stoychev, S. D.; Kuleff, A. I.; Chiang, Y.-C.; Gokhberg, K.; Kopelke, S.; Sisourat, N.; et al. Interatomic electronic decay processes in singly and multiply ionized clusters. *J. Electron Spectrosc. Relat. Phenom.* **2011**, *183*, 36.

(8) Jahnke, T. Interatomic and intermolecular Coulombic decay: the coming of age story. *J. Phys. B: At., Mol. Opt. Phys.* **2015**, *48*, 082001.

(9) Zobeley, J.; Santra, R.; Cederbaum, L. S. Electronic decay in weakly bound heteroclusters: Energy transfer versus electron transfer. *J. Chem. Phys.* **2001**, *115*, 5076–5088.

(10) Müller, I. B.; Cederbaum, L. S. Electronic decay following ionization of aqueous Li$^+$ microsolvation clusters. *J. Chem. Phys.* **2005**, *122*, 094305.

(11) Sakai, K.; Stoychev, S.; Ouchi, T.; Higuchi, I.; Schöffler, M.; Mazza, T.; Fukuzawa, H.; Nagaya, K.; Yao, M.; Tamenori, Y.; et al. Electron-Transfer-Mediated Decay and Interatomic Coulombic Decay from the Triply Ionized States in Argon Dimers. *Phys. Rev. Lett.* **2011**, *106*, 33401.

(12) Förstel, M.; Mucke, M.; Arion, T.; Bradshaw, A. M.; Hergenhahn, U. Autoionization Mediated by Electron Transfer. *Phys. Rev. Lett.* **2011**, *106*, 033402.

(13) Santra, R.; Cederbaum, L. S. Non-Hermitian electronic theory and applications to clusters. *Phys. Rep.* **2002**, *368*, 1–117.

(14) Jahnke, T.; Czasch, A.; Schöffler, M.; Schössler, S.; Käsz, M.; Titze, J.; Kreidi, K.; Grisenti, R. E.; Staudte, A.; Jagutzki, O.; et al. Experimental Separation of Virtual Photon Exchange and Electron Transfer in Interatomic Coulombic Decay of Neon Dimers. *Phys. Rev. Lett.* **2007**, *99*, 153401.

(15) Barth, S.; Marburger, S. P.; Joshi, S.; Ulrich, V.; Kugeler, O.; Hergenhahn, U. Interface Identification by Non-Local Autoionization Transitions. *Phys. Chem. Chem. Phys.* **2006**, *8*, 3218–3222.

(16) Aziz, E. F.; Ottosson, N.; Faubel, M.; Hertel, I. V.; Winter, B. Interaction Between Liquid Water and Hydroxide Revealed by Core-Hole Deexcitation. *Nature* **2008**, *455*, 89–91.

(17) Pokapanich, W.; Bergersen, H.; Bradeanu, I. L.; Marinho, R. R. T.; Lindblad, A.; Legendre, S.; Rosso, A.; Svensson, S.; Björneholm, O.; Tchaplyguine, M.; et al. Auger Electron Spectroscopy as a Probe of the Solution of Aqueous Ions. *J. Am. Chem. Soc.* **2009**, *131*, 7264–7271.

(18) Pokapanich, W.; Ottosson, N.; Svensson, S.; Öhrwall, G.; Winter, B.; Björneholm, O. Bond Breaking, Electron Pushing, and Proton Pulling: Active and Passive Roles in the Interaction between Aqueous Ions and Water as Manifested in the O 1s Auger Decay. *J. Phys. Chem. B* **2012**, *116*, 3–8.

(19) Grieves, G. A.; Orlando, T. M. Intermolecular Coulomb Decay at Weakly Coupled Heterogeneous Interfaces. *Phys. Rev. Lett.* **2011**, *107*, 016104.

(20) Fasshauer, E.; Förstel, M.; Pallmann, S.; Pernpointner, M.; Hergenhahn, U. Using ICD for Structural Analysis of Clusters: A Case Study on NeAr Clusters. *New J. Phys.* **2014**, *16*, 103026.

(21) Lundwall, M.; Pokapanich, W.; Bergersen, H.; Lindblad, A.; Rander, T.; Öhrwall, G.; Tchaplyguine, M.; Barth, S.; Hergenhahn, U.; Svensson, S.; et al. Self-Assembled Heterogeneous Argon/Neon Core-Shell Clusters Studied by Photoelectron Spectroscopy. *J. Chem. Phys.* **2007**, *126*, 214706–214708.

(22) Lengen, M.; Joppien, M.; Müller, R.; Wörmer, J.; Möller, T. Site-specific excitation and decay processes in XeAr$_N$ clusters. *Phys. Rev. Lett.* **1992**, *68*, 2362.

(23) Lengen, M.; Joppien, M.; von Pietrowski, R.; Möller, T. Assignment of Impurity States in Xenon-Doped Argon Clusters. *Chem. Phys. Lett.* **1994**, *229*, 362–369.

(24) Tchaplyguine, M.; Lundwall, M.; Gisselbrecht, M.; Öhrwall, G.; Feifel, R.; Sorensen, S.; Svensson, S.; Martensson, N.; Björneholm, O. Variable Surface Composition and Radial Interface Formation in Self-

Assembled Free, Mixed Ar/Xe Clusters. *Phys. Rev. A: At., Mol, Opt. Phys.* 2004, 69, 031201R.

(25) Hoener, M.; Bostedt, C.; Thomas, H.; Landt, L.; Eremina, E.; Wabnitz, H.; Laarmann, T.; Treusch, R.; Castro, A. R. B. d.; Möller, T. Charge Recombination in Soft X-Ray Laser Produced Nanoplasmas. *J. Phys. B: At., Mol. Opt. Phys.* 2008, 41, 181001.

(26) Danylchenko, O.; Doronin, Y.; Kovalenko, S.; Samovarov, V. Phase Separation into Pure Components in Mixed Ar-Xe Clusters. *JETP Lett.* 2006, 84, 324–328.

(27) Danylchenko, O. G.; Doronin, Y. S.; Kovalenko, S. I.; Libin, M. Y.; Samovarov, V. N.; Vakula, V. L. Luminescence Evidence for Bulk and Surface Excitons in Free Xenon Clusters. *Phys. Rev. A: At., Mol., Opt. Phys.* 2007, 76, 043202.

(28) Lindblad, A.; Rander, T.; Bradeanu, I.; Öhrwall, G.; Björneholm, O.; Mucke, M.; Ulrich, V.; Lischke, T.; Hergenhahn, U. Chemical Shifts of Small Heterogeneous Ar/Xe Clusters. *Phys. Rev. B: Condens. Matter Phys.* 2011, 83, 125414.

(29) von Pietrowski, R.; von Haeften, K.; Laarmann, T.; Möller, T.; Museur, L.; Kanaev, A. V. Electronic and Geometric Structure of Doped Rare-Gas Clusters: Surface, site and size effects studied with luminescence spectroscopy. *Eur. Phys. J. D* 2006, 38, 323–336 and references therein.

(30) Lindblad, A.; Bergersen, H.; Rander, T.; Lundwall, M.; Öhrwall, G.; Tchaplyguine, M.; Svensson, S.; Björneholm, O. The Far from Equilibrium Structure of Argon Clusters Doped with Krypton or Xenon. *Phys. Chem. Chem. Phys.* 2006, 8, 1899–1905.

(31) Marques, J. M. C.; Pereira, F. B. A Detailed Investigation on the Global Minimum Structures of Mixed Rare-Gas Clusters: Geometry, Energetics, and Site Occupancy. *J. Comput. Chem.* 2013, 34, 505–517.

(32) Vach, H. Impurity Dynamics in Binary van der Waals Clusters Created by Pick-Up. *J. Chem. Phys.* 1999, 111, 3536–3547.

(33) Fasshauer, E.; Kryzhevoi, N. V.; Pernpointner, M. Possible Electronic Decay Channels in the Ionization Spectra of Small Clusters Composed of Ar and Xe: A Four-Component Relativistic Treatment. *J. Chem. Phys.* 2010, 133, 014303.

(34) Fasshauer, E.; Pernpointner, M.; Gokhberg, K. Interatomic Decay of Inner-Valence Ionized States in ArXe Clusters: Relativistic Approach. *J. Chem. Phys.* 2013, 138, 014305.

(35) Hagena, O. F. Cluster Ion Sources. *Rev. Sci. Instrum.* 1992, 63, 2374–2379.

(36) Arion, T.; Mucke, M.; Förstel, M.; Bradshaw, A. M.; Hergenhahn, U. Interatomic Coulombic Decay in Mixed NeKr Clusters. *J. Chem. Phys.* 2011, 134, 074306.

(37) Danylchenko, O. G.; Kovalenko, S. I.; Konotop, O. P.; Samovarov, V. N. Diagnostics of Composition and Size of Clusters Formed in Supersonic Jets of ArKr Gas Mixtures. *Low Temp. Phys.* 2015, 41, 637–644.

(38) Lundwall, M.; Tchaplyguine, M.; Öhrwall, G.; Feifel, R.; Lindblad, A.; Lindgren, A.; Sörensen, S.; Svensson, S.; Björneholm, O. Radial Surface Segregation in Free Heterogeneous Argon/Krypton Clusters. *Chem. Phys. Lett.* 2004, 392, 433–438.

(39) Bergersen, H.; Abu-Samha, M.; Harnes, J.; Björneholm, O.; Svensson, S.; Sæthre, L. J.; Børve, K. J. Size of Neutral Argon Clusters from Core-Level Photoelectron Spectroscopy. *Phys. Chem. Chem. Phys.* 2006, 8, 1891–1898.

(40) Hergenhahn, U.; Barth, S.; Ulrich, V.; Mucke, M.; Joshi, S.; Lischke, T.; Lindblad, A.; Rander, T.; Öhrwall, G.; Björneholm, O. 3p Valence Photoelectron Spectrum of Ar Clusters. *Phys. Rev. B: Condens. Matter Mater. Phys.* 2009, 79, 155448.

(41) Förstel, M.; Mucke, M.; Arion, T.; Lischke, T.; Barth, S.; Ulrich, V.; Öhrwall, G.; Björneholm, O.; Hergenhahn, U.; Bradshaw, A. M. Energy Band Dispersion in Photoemission Spectra of Argon Clusters. *J. Electron Spectrosc. Relat. Phenom.* 2011, 184, 107–112.

(42) Mucke, M.; Förstel, M.; Lischke, T.; Arion, T.; Bradshaw, A. M.; Hergenhahn, U. Performance of a Short 'Magnetic Bottle' Electron Spectrometer. *Rev. Sci. Instrum.* 2012, 83, 063106.

(43) Förstel, M. Investigation of Non-Local Autoionization Processes in Rare Gas Clusters. Ph.D. thesis, Technical University Berlin, 2012; http://opus.kobv.de/tuberlin/volltexte/2012/3656/.

(44) Fasshauer, E. Investigation of Relativistic Effects in Electronic Decay Processes in Small and Large Noble Gas Clusters by Ab Initio and New Simulation Approaches. Ph.D. thesis, University of Heidelberg, 2014.

(45) Wentzel, G. Über Strahlungslose Quantensprünge. *Eur. Phys. J. A* 1927, 43, 524–530.

(46) Feshbach, H. Unified Theory of Nuclear Reactions. *Ann. Phys.* 1958, 5, 357–390.

(47) Feshbach, H. A Unified Theory of Nuclear Reactions. II. *Ann. Phys.* 1962, 19, 287–313.

(48) Fano, U. Effects of Configuration Interaction on Intensities and Phase Shifts. *Phys. Rev.* 1961, 124, 1866–1878.

(49) Fasshauer, E. *HARDRoC*, Hunting Asymptotic Relativistic Decay Rates of Clusters, 2013; http://www.pci.uni-heidelberg.de/tc/usr/elke/hardroc/html/main.html.

(50) Haberland, H. *Clusters of Atoms and Molecules Theory, Experiment, and Clusters of Atoms*; Springer Series in Chemical Physics; Springer: Berlin/Heidelberg, 1994; p 422.

(51) *Avogadro*, An Open-Source Molecular Builder and Visualization Tool, Version 1.1.0; http://avogadro.openmolecules.net.

(52) Hanwell, M. D.; Curtis, D. E.; Lonie, D. C.; Vandermeersch, T.; Zurek, E.; Hutchison, G. R. Avogadro: An Advanced Semantic Chemical Editor, Visualization, and Analysis Platform. *J. Cheminf.* 2012, 4, 17.

(53) Herman, P. R.; LaRocque, P. E.; Stoicheff, B. P. Vacuum Ultraviolet Laser Spectroscopy. V. Rovibronic Spectra of Ar_2 and Constants of the Ground and Excited States. *J. Chem. Phys.* 1988, 89, 4535–4549.

(54) Freeman, D. E.; Yoshino, K.; Tanaka, Y. Vacuum Ultraviolet Absorption Spectrum of the van der Waals Molecule Xe_2. I. Ground State Vibrational Structure, Potential Well Depth, and Shape. *J. Chem. Phys.* 1974, 61, 4880–4889.

(55) Mucke, M. Employing Electron-Electron Coincidence Techniques to Investigate the Autoionisation of Clusters. Ph.D. thesis, Technical University Berlin, 2011; http://opus.kobv.de/tuberlin/volltexte/2011/3073/.

(56) Schnorr, K.; Senftleben, A.; Schmid, G.; Augustin, S.; Kurka, M.; Rudenko, A.; Foucar, L.; Broska, A.; Meyer, K.; Anielski, D.; et al. Time-Resolved Study of ICD in Ne Dimers Using FEL Radiation. *J. Electron Spectrosc. Relat. Phenom.* 2015, 204, 245.

(57) Fasshauer, E. Non-Nearest Neighbour ICD in Clusters. *New J. Phys.* 2016, 18, 043028.

(58) Samson, J. A. R.; Stolte, W. C. Precision Measurements of the Total Photoionization Cross-Sections of He, Ne, Ar, Kr, and Xe. *J. Electron Spectrosc. Relat. Phenom.* 2002, 123, 265–276.

(59) Velchev, I.; Hogervorst, W.; Ubachs, W. Precision VUV Spectroscopy of Ar I at 105 nm. *J. Phys. B: At., Mol. Opt. Phys.* 1999, 32, L511.

(60) Sansonetti, J. E.; Martin, W. C. Handbook of Basic Atomic Spectroscopic Data. *J. Phys. Chem. Ref. Data* 2005, 34, 1559–2259.

(61) Rolles, D.; Zhang, H.; Pesic, Z. D.; Bozek, J. D.; Berrah, N. Emergence of Valence Band Structure in Rare-Gas Clusters. *Chem. Phys. Lett.* 2009, 468, 148–152.

(62) Förstel, M.; Mucke, M.; Arion, T.; Lischke, T.; Barth, S.; Ulrich, V.; Öhrwall, G.; Björneholm, O.; Hergenhahn, U.; Bradshaw, A. M. Observation of Electronic Energy Bands in Argon Clusters. *Phys. Rev. B: Condens. Matter Mater. Phys.* 2010, 82, 125450.

(63) Jacobi, K.; Rotermund, H. UV Photoemission from Physisorbed Atoms and Molecules: Electronic Binding Energies of Valence Levels in Mono- and Multilayers. *Surf. Sci.* 1982, 116, 435–455.

(64) Jacobi, K. Photoemission from Ar, Kr, and Xe on Pb(111). *Phys. Rev. B: Condens. Matter Mater. Phys.* 1988, 38, 5869–5877.

(65) Hergenhahn, U.; Kolmakov, A.; Riedler, M.; de Castro, A. R. B.; Löfken, O.; Möller, T. Observation of excitonic satellites in the photoelectron spectra of Ne and Ar clusters. *Chem. Phys. Lett.* 2002, 351, 235–241.

(66) Feifel, R.; Tchaplyguine, M.; Öhrwall, G.; Salonen, M.; Lundwall, M.; Marinho, R. R. T.; Gisselbrecht, M.; Sorensen, S. L.; Naves de Brito, A.; Karlsson, L.; et al. From Localised to Delocalised

Electronic States in Free Ar, Kr and Xe Clusters. *Eur. Phys. J. D* **2004**, *30*, 343−351.

(67) Zhang, H.; Rolles, D.; Pesic, Z. D.; Bozek, J. D.; Berrah, N. Angular Distributions of Inner-Shell Photoelectrons from Rare-Gas Clusters. *Phys. Rev. A: At., Mol, Opt. Phys.* **2008**, *78*, 063201.

(68) Kruit, P.; Read, F. H. Magnetic Field Paralleliser for 2π Electron-Spectrometer and Electron-Image Magnifier. *J. Phys. E: Sci. Instrum.* **1983**, *16*, 313−324.

(69) Mucke, M.; Braune, M.; Barth, S.; Förstel, M.; Lischke, T.; Ulrich, V.; Arion, T.; Becker, U.; Bradshaw, A.; Hergenhahn, U. A Hitherto Unrecognized Source of Low-Energy Electrons in Water. *Nat. Phys.* **2010**, *6*, 143−146.

(70) Förstel, M.; Arion, T.; Hergenhahn, U. Measuring the Efficiency of Interatomic Coulombic Decay in Ne Clusters. *J. Electron Spectrosc. Relat. Phenom.* **2013**, *191*, 16−19.

(71) Fasshauer, E.; Förstel, M.; Mucke, M.; Arion, T.; Hergenhahn, U., to be published.